Study of $\sqrt{2}$ Conjecture in the Construction of Drag Induced Wind Turbine Blade Morphology

S.N. Ashwindran[1], A.A. Azizuddin[2,*] A.N. Oumer[3]

[1,2,3] Faculty of Mechanical and Automotive Engineering Technology, Universiti Malaysia Pahang, Malaysia

*Author to whom correspondence should be addressed:
E-mail: azizuddin@ump.edu.my

(Received February 3, 2021; Revised May 12, 2021; accepted July 6, 2021).

Abstract: In wind engineering, the morphology of the turbine blade system governs the effectiveness in harvesting wind energy. The flow field response is the result of the turbine blade shape interaction with flow. Hence, mathematically interpreting the shape of the blade will help to understand the principals and properties of the utilized geometry for the blade construction. In this study, semicircle geometry of Savonius wind turbine blade is mathematically analyzed in order to understand its fundamental building block. We provide discussion on $\sqrt{2}$ conjecture found in the construction of circles, Fibonacci and Pythagoras spiral in relations to $\sqrt{2}, \sqrt{2}+1$ and $\sqrt{2}+2$. It is found that $\sqrt{2}$ conjecture can be utilized in determining the geometrical properties of circle and spiral. We also performed thorough assessment of the proposed conjecture to prove its robustness and reliability. The proposed conjecture is adapted to construct the blade morphology of drag induced wind turbine. CFD analysis is carried out to investigate the aerodynamic properties namely moment coefficient (C_m) of the constructed wind turbine shape via the proposed conjecture. Results shows that the proposed shape constructed based on the conjecture has improved C_m by 7.2 % at λ = 0.59 and 4 % at λ = 0.94 compared to conventional SWT.

Keywords: Savonius wind turbine; blade morphology; irrational number

1. Introduction

Elements in nature are ubiquitously and aesthetically constructed by patterns and algorithmic shapes that represents a hidden mathematical notion. The mysteries of hidden geometries in nature can be deduced and expressed in mathematical terms in order to understand nature sense of symmetry and building block of geometrical order. In general terms, there are 3 types of pattern configuration namely fractals, spiral and Voronoi. Patterns in nature exhibit higher order of complex symmetrical properties. Symmetrical order is classified into two types which are bilateral and rotational symmetry[1)]. Mathematicians define symmetry as numerical order that is invariant to transformation such as rotation, translation and reflection [2)]. Lin (1996) [3)] stated that symmetry represents the state of orderliness in a pattern configuration. Naturally reoccurring patterns exhibit similarity at different level and scale such as Mandelbrot set [4)]. It means that patterns are set of shapes that repeat in identical manner without being in random configuration [5)]. Mathematically interpreting symmetrical pattern phenomena helps to understand the principal of defining shapes exhibited by nature. In special cases, group theory method is utilized to analyze the complexity of symmetrical patterns. Symmetry shapes inspire manmade work of art such as architecture [6)], textile [7)], ornament [8)] and art [9)]. The widely renowned numerical value phi denotes by the symbol of ϕ or φ is often found in most of the natural patterns. Phi is also known as the golden ratio, where the approximate value is 1.6180. The mathematical derivation of golden ratio fascinates intellectuals from various fields for at least 2400 years [10)]. In mathematical term, golden ratio is considered as irrational number due to its large number of decimal places. In other words, the value of irrational number cannot be obtained by the division of two integers [11)]. However, scientists found that golden ratio is overestimated in art and nature since the measurement does not comply to standard methodology and it is impossible to measure complex structures with accuracy [12)].

Similarly, there are other irrational numbers widely used in the field of mathematics namely Pi (the ratio of circumference to the diameter of the circle, π) and e (exponential function of an argument). It is observed that irrational number such as π, e and ϕ have infinite number of decimal digits, hence for simplicity the value is approximated to 4-5 decimal digits. Sen & Agarwal (2008) [13)] stated that rational and irrational number-π plays an important role in computer science and mathematics. Interestingly, golden ratio is also utilized for various business and management optimal search method

purposes [14]. Fibonacci sequence is utilized for solving issues on inventory and quality control [15]. While investigating issues on inventory and production, Disney et al., (2004) [16] observed that utilization of golden ratio method has reduced sum of inventory and order of variance over time. This supports the fact that transcendental number can be utilized in various field of research as an analytical toll. In mathematics, irrational means are grouped as metallic ratios consisting of gold, silver and bronze ratio. Each of the ratio is linked to a particular numerical sequence; golden ratio is related to Fibonacci sequence; silver ratio (δ_s) is linked to Pell number; bronze ratio is connected to on-line encyclopaedia of integer sequence (OEIS). It is worth mentioning that these ratios and sequence are the hidden fundamental element that dictates the behaviour and growth pattern of geometries. Conventionally, π related formulations are utilized to determine the parameters of the circles and spirals. However, it is observed that $\sqrt{2}$ conjecture exist in these geometries as well.

In regards to engineering application, the morphology of a system determines its performance and dictates its interaction behaviour namely aerofoil morphology [17], liquid transportation system [18], heat transfer system and others. Similarly, in wind engineering the aerodynamics performance of a wind turbine (WT) in capturing wind kinetic energy is majorly dependent on the morphology of the blade. The blade shape influences the flow field properties and the behaviour of flow response. Traditional WT design struggles with fundamental design error which consequently impacted the operational capabilities. Compounded structural design issues namely blade structure constitutes to the inefficiency of the WT [19]. Despite over 30 years of experience, manufacturers and engineers are adherently working to improve the efficiency of WT [19]. In spite of other improvements namely material structure, gearbox modification, turbine and control system enhancement in WT technology, less attention is paid to blade morphology design. Traditional WT design and mechanism are investigated based on past studies presented by researchers, in order to understand the governing factors that influence the aerodynamic performance. It is found that conventional blade design of WT is incapable to extract more wind energy due to its blade shape. However, the complexity of WT behavior and flow properties can be analyzed via numerical Computational fluid dynamic (CFD) model. In recent years, CFD strategies has grown into a prominent tool of analysis for complex flow related scenarios[20].

Conventional Savonius turbine is adapted for this study, where the blade shape is geometrically analyzed in order to understand the aerodynamics performance of WT relative to the blade shape. In this study, semicircle geometry of Savonius turbine is mathematically analyzed in order to understand the reasoning behind the construction of circle. Previous computational fluid dynamics (CFD) studies on the investigation of Savonius turbine indicate that reduction in blade height increases the effectiveness energy harvesting [21]. Hence this paper presents the developed numerical methodology based on $\sqrt{2}$ conjecture which is utilized for the construction of the proposed Savonius turbine blade.

2. Literature survey

2.1 Golden ratio

Geometrically, golden mean is the ratio of the whole segment to the longer segment where the value is equal to the ratio of the longer segment to the shorter segment as illustrated in Figure 1 and Equation 1. The precise value is 1.6180339887…., an infinite non-recurring number [22]. Due to the exhibited numerical properties, golden ratio cannot be expressed in fraction whole number, hence considered as an irrational number [23]. Equation 2 shows the quadratic expression of Equation 1, where the positive quadratic root as expressed in Equation 3 is equal to golden ratio. Interestingly, when the value of golden ratio is subtracted with one, the value is equal to its reciprocal as shown in Equation 4. Moreover, the result via Euler continued fraction method equals to golden ratio as shown in Equation 5 [24].

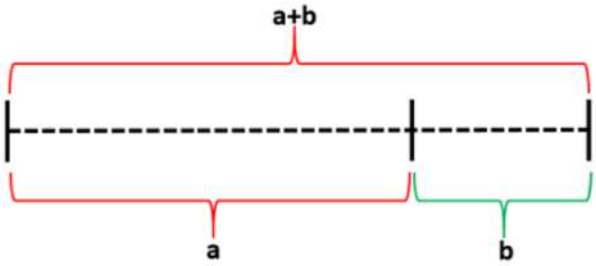

Fig. 1: Illustration of golden ratio by line segments.

$$\frac{a+b}{a} = \frac{a}{b} = \phi \tag{1}$$

$$a^2 - ab - b^2 = 0 \tag{2}$$

$$\phi = \frac{1+\sqrt{5}}{2} = 1.6180339887..... \tag{3}$$

$$1 - \phi = \frac{1}{\phi} = 0.6180339887 \tag{4}$$

Euler continued fraction of ϕ,

$$\phi = 1 + \cfrac{1}{1 + \cfrac{1}{1 + \cfrac{1}{1 + \cfrac{1}{1 + \cfrac{1}{1 + \cfrac{1}{1+\ddots}}}}}} \tag{5}$$

2.2 Fibonacci sequence

Fibonacci sequence and golden ratio are closely related in the construction of geometrical patterns namely golden rectangle and spiral. In simple terms, the behaviour of Fibonacci (F_n) sequence is often expressed as quadratic recursive as shown in Equation 6 [25]. The sequence of Fibonacci can be formed with any integer more $n \geq 2$, where the number formed is the sum of the preceding numbers. Fibonacci sequence frequently appears in geometry and pattern in nature namely sunflower florets, pinecone spiral, nautilus shell and others. The Fibonacci spiral or otherwise logarithmic spiral is generated by the growth factor to golden ratio. Fibonacci spiral as shown in Figure 2 is formed by the arc connecting two points of the square constructed based on the sequence as shown in Equation 7. Fibonacci sequence is widely used in various field of study which exhibits asymptotic behaviour and can be described through linear recurrence [26].

$$F_n = F_{n+1} + F_{n-2} \tag{6}$$

$$F_n = 0, 1, 1, 2, 3, 5, 8, 13, 21, 34, 55..... \tag{7}$$

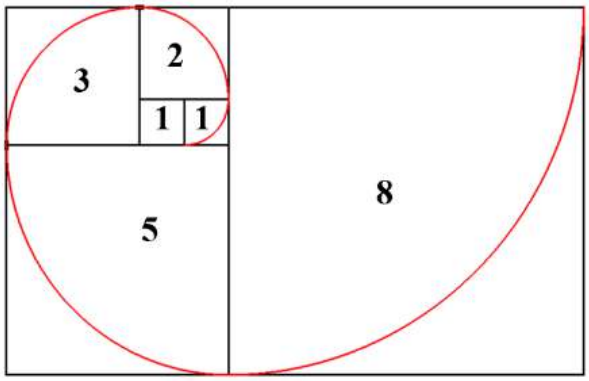

Fig 2: Construction of Fibonacci spiral.

It is worth mentioning that similar sequential properties can be observed in mathematical methodology developed by French mathematician, Blaise Pascal. Figure 3 shows the array of generalized Pascal triangle, where the sum of diagonal number is similar to Fibonacci sequence [27]. Pascal triangle is used to determine the combination problems in probability. As illustrated in Figure 3, Pascal triangle exhibits symmetrical properties, where the numbers on left and right side of triangle are identical. In general terms, binominal expression is the sum or difference of two terms. Interestingly, in the coefficient of a binominal expansion of $(a+b)^n$, the n coefficient can be identified from the n_{th} row of Pascal triangle. Binomial theorem can be represented as expressed in Equation 8-9.

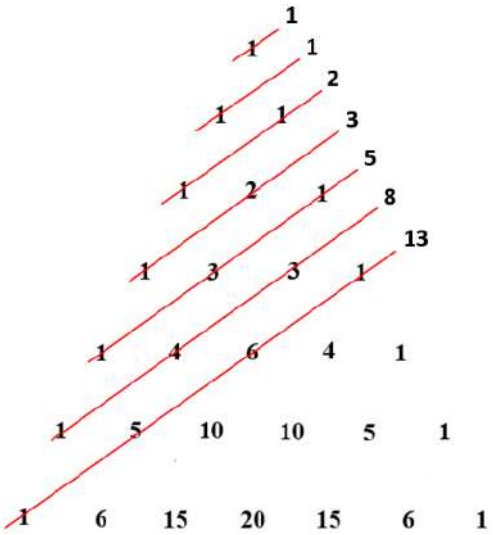

Fig 3: Fibonacci sequence in generalized Pascal triangle.

$$a_{nr} \equiv \frac{n!}{r!\,(n-r)!} \equiv \binom{n}{r} \tag{8}$$

$$\binom{n}{r} = \frac{n!}{r!\,(n-r)!} = \binom{n-1}{r} + \binom{n-1}{r-1} \tag{9}$$

As aforementioned, golden ratio is associated in the growth of Fibonacci spiral. The ratio of the successive number to the preceding number approximately converges to golden ratio as reported in Table 1 [13]. Fibonacci sequence has fundamentally associated with several other prominent mathematical methodologies namely Lucas number [28], Fermat theorem [29], Pascal triangle [30], Mandelbrot set [31], and Pell number [32].

Table 1. Fibonacci sequence and ratio.

Terms	F_n	F_n (n-1)	F_n/F_n (n-1)
1	1.00	1.00	1.00000
2	2.00	1.00	2.00000
3	3.00	2.00	1.50000
4	5.00	3.00	1.66667
5	8.00	5.00	1.60000
6	13.00	8.00	1.62500
7	21.00	13.00	1.61538
8	34.00	21.00	1.61905
9	55.00	34.00	1.61765
10	89.00	55.00	1.61818
11	144.00	89.00	1.61798

2.3 Geometrical ratio inspired WT

It is evident that geometrical driven numerical ratio has proven to be effective as it is being implement in the development of mechanical system. Zheng et al., (2019) investigated the aerodynamic performance of resistant type vertical axis wind turbine inspired Nautilus isometric spiral configuration[33]. The author utilized Simulink to construct a numerical model to investigate the power generation characteristic of the WT. The author concluded that the optimized performance of the WT can be obtained with three blades and optimal size ratio of 0.76. Patil. (2018) carried out CFD and experimental analysis on horizontal axis wind turbine (HAWT) inspired by Fibonacci spiral [34]. The author claimed that spiral inspired WT configuration is highly efficient and able to extract 80 % of wind power in contrast to conventional WT. Lu et al., (2012) [35] numerically and theoretical investigated the aerodynamic performance of spiral inspired HAWT. The theoretical value is compared with numerical simulation conducted using ANSYS CFX v12.1. The author mentioned that the presented configuration is able to achieve maximum efficiency. Monatrakul et al., (2017) conducted study on spiral hydro turbine[36]. The author concluded that spiral horizontal turbine is suitable for low velocity fluid flow due to its strand shape. Moreover, spiral configured turbine is highly effective in intercepting the kinetic energy of the flow fluid [37]. Meanwhile, Suntivarakorn et al., (2016) developed a horizontal spiral turbine based on golden ratio function [38]. The author mentioned that the proposed turbine showed an efficiency of 48 % which is 15 % higher than propeller-based turbine.

2.4 Past studies on wind turbine CFD configuration

Antar & Elkhoury. (2019) [39] work on improving the performance of SWT using CFD analysis in order to obtain the appropriate size for rotor guide plate. ANSYS Fluent is used for the CFD numerical study. The author declared that SST *k-ω* is highly recommended for predicting flow around SWT. Moreover, the author endorsed SST *k-ω* due to the fact that, it is more suitable for external aerodynamics flow numerical simulations namely flow over energy harvesting devices in contrast to RNG, realizable and standard *k-ε*. The author concluded that result from 2D simulation overestimated experimental data in terms of C_p. However, the author justified that 2D simulation is less burdening in comparison to 3D model with complex parametric configuration. He et al. (2020) [40] presented an aerodynamic study of VAWT in order to investigate on the reliability and accuracy several CFD numerical techniques such as 2D URANS, 2.5D URANS, 3D URANS, 2.5D large eddy simulation (LES), and 3D LES. The mesh topology of the configurations is generated using ICEM, based on SMM in order to allow data exchange between adjacent flow fields. In order to obtain 2.5D configuration, the 2D model is extended in spanwise direction but less than the actual blade length.

Celik et al. (2020) [41] investigated H-rotor type VAWT self-starting behavior via CFD numerical analysis. In terms of CFD configuration, the simulation is based on pressure-based solver using SIMPLE algorithm as for pressure-velocity coupling. In terms of spatial discretization, green gauss node is applied for gradient and pressure and momentum is set to second order upwind. Since the paraments on turbulent intensity is unknown in the experimental study, therefore the author utilized 1% and 10% for turbulent intensity and turbulent viscosity (β) respectively. Based on the author's past study, it is found that SST *k-ω* is widely endorsed by several author due to its capabilities. Hence the author chose to proceed the simulations with SST *k-ω* turbulent transport model. Mauro et al., (2019) [42] studied the behavior of ducted SWT via CFD analysis in 2D configuration. The author validated the CFD result against data gather from experimental procedure conducted in subsonic wind tunnel. The author employed sliding mesh model (SMM) to initiate rotation of the 2D WT domain in ANSYS Fluent. The author mentioned that URANS model is highly recommended for cases with low Reynolds number. In terms of mesh topology, the discretized grid meets the requirement of $Y^+ < 1$. The author claimed that PISO algorithm is more efficient and the convergence criteria is faster and more reliable in contrast to SIMPLE and couple algorithm. Moreover, author stated that *k-ε*, *k-ω* and SST *k-ω* is not suitable and conceptually incorrect since the simulation is govern by high transitional effects. Hence, the simulation is carried out based on transition SST model as for turbulent transport model.

2.5 Savonius wind turbine

There are two basic blade morphologies for WT namely guide cavity vane and aerofoil. The blade of conventional WT is a semi-circular structure as shown in Figure. As for aerodynamic profile, guide cavity vane blades are considered as drag based. In the matter of configuration for axis of rotation, Savonius WT is considered as vertical axis wind turbine (VAWT). In precis of historical timeline of wind blade design, Fausto Veranzio in 1616 from Venetian Republic (Modern Croatia) presented several types of windmill blade designs in his book titled "Machinae Novae" [43]. Later on, Finish inventor Sigurd Johannes Savonius patented the Savonius WT in 1927 [44]. Soon after, several other designs of WT guide cavity vane and modified Savonius blades were introduced. Figure 4 shows the traditional parametric design attributes of Savonius turbine.

Conventionally, parametric modification is made on overlap ratios (*OR*) and aspect ratio of the turbine design in order to improve the performance. Aspect ratio of the turbine is the ratio of the rotor diameter (D_R) to turbine height (H). However, less attention is paid on the blade morphology and blade height (h). Previous study showed that adjustment in blade height and blade curvature improves the effectiveness in torque generation.

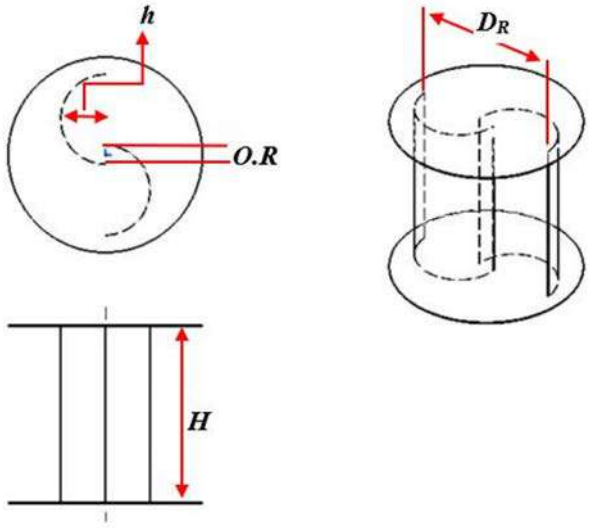

Fig 4: Savonius blade geometry.

3. Methodology

3.1 Shape factor of circle

Definition 3.1. Let length $\overline{PC}$ (*x*,*y*) defined as $L_{pr\text{-}sq}$, be an arbitrary line segment of a square, $\overline{PC}$ = *a* as manifested in Figure 5. Suppose there is an intersection point between the arc of the circle and the line of segment of the square. Point *C* (*x*,*y*) of line $\overline{PC}$ lies on the circumference of the arc. **Remark:** The units of the parameters is set to meter (m).

Definition 3.2 The constructed square based on the line segment $\overline{PC}$ is defined as primary square. Since the construction is initiated with primary square, the arc is tangential to line passing point *C* as illustrated in Figure 5. In other words, point *C* of the primary square is positioned 45 º to tangent line of the arc and 135 º to the radius line which is connecting to the center point of the arc.

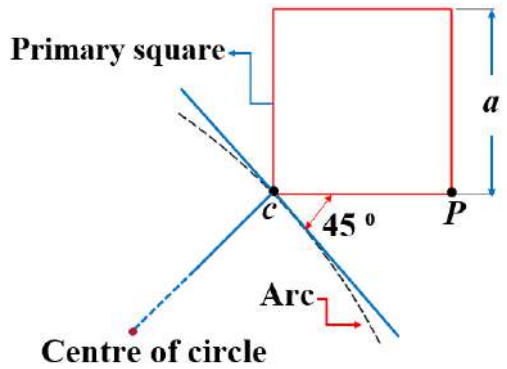

Fig 5: Line segment of a square at arbitrary length.

Proposition 3.3. Assuming an arbitrary length $\overline{PC}$ (*x*,*y*) of a quadrilateral is (5,0), where point *C* (*x*,*y*) = (12.07,12.07) lies on the circumference of the circle. Assuming the relationship is linear, the radius (*r*) of the circle is the product of factor length segment [$\overline{PC}$] to constant *k* as shown in Equation 10. **Remark**. The smaller square is denoted as the primary and the overlapping larger square is secondary as shown in Figure 6. The secondary square has to cover the arc of a circle quadrant.

$$R = k\left(\overline{PC}\right) \tag{10}$$

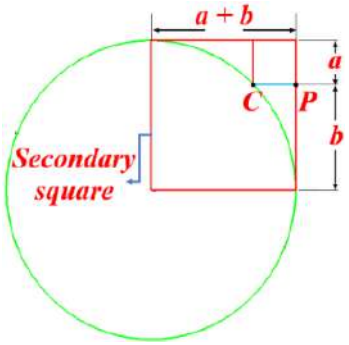

Fig 6: Illustration on the construction of circle and square.

Proof. It is found that the radial and bilateral growth of quadrants forming in to a circle is based on $\sqrt{2}$ as shown in Figure 7. The ratios are shown in Equation 10-11.

$$\frac{a+b}{b},\ \frac{b}{a},\ \frac{a+b}{a} \tag{11}$$

$$\left(\frac{17.07}{12.07} \approx 1.4142 \approx \sqrt{2}\right), \left(\frac{12.07}{5.0} \approx 2.41422 \approx \sqrt{2}+1\right),$$

$$\left(\frac{17.07}{5.0} \approx 3.414 \approx \sqrt{2}+2\right)$$

$$\sqrt{2},\ \sqrt{2}+1,\ \sqrt{2}+2$$

Note. Meanwhile the Chord length of the quadrant (*Cl-quad*), diagonal length of the primary square ($Dl_{p\text{-}sq}$).
Definition 3.4. $C_{l-quad} = \left(\sqrt{2}+2\right) \times Dl_{p-sq}$, $C_{l\text{-}qua}$ also can be calculated using $\sqrt{2}+1$ as shown in Figure 7.
Theorem 3.1. Given that $Dl_{P-sq} = \overline{PC} \times \sqrt{2} \approx 7.07$,
Proof. Then $C_{l-qua} = 7.07 \times \left(\sqrt{2}+2\right) \approx 24.14$, meanwhile in terms of $\sqrt{2}+1$, $C_{l-qua} = 5 \times \left(\left(\sqrt{2}+1\right) \times 2\right) \approx 24.14$. In terms of $\sqrt{2}$, $C_{l-qua} = 7.07 \times \sqrt{2} \approx 24.14$,

Therefore, the radius of the circle is $r = \frac{C_{l-qua}}{\sqrt{2}} =$

$\frac{24.14}{\sqrt{2}} = 17.07$, or $5.0 * \left(\sqrt{2}+2\right) \approx 17.07$.

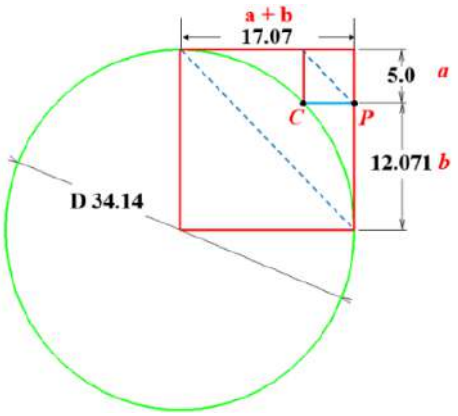

Fig 7: Construction of $\sqrt{2}$ in a circle.

Note. The length or arc of a segment is denoted as ($L_{a\text{-}seg}$) and length of arc of quadrant ($L_{a\text{-}qua}$). **Definition 3.5**. As shown in Equation 13, the relationship between $C_{l\text{-}qua}$ and $L_{a\text{-}qua}$ is analyzed in terms of ratio and angle relative to π. **Remark**. The ratio k is depended on angle of the sector.

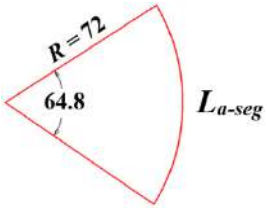

Fig 8: Sector of a circle of angle 64.8º.

3.2 Shape factor of spiral

It is observed that $\sqrt{2}$ conjecture appears in the construction of Fibonacci spiral. Hence, Fibonacci spiral configuration is constructed based on the proposed conjecture as shown in Equation 12. Fibonacci number consequently from a set of infinite sequence, where the proceeding number is the sum of two previous number [13]. The Fibonacci spiral or otherwise logarithmic spiral is generated by the growth factor of ((1+ $\sqrt{5}$) / 2) converging to golden ratio [45].

$$F_n = 0, 1, 1, 2, 3 \ldots \quad (12)$$

Definition 3.6. Let Fibonacci sequence be the radius of the arc in the spiral configuration. As shown in Figure 9, the dimension of the inner square intersecting the arc is the ratio of Fibonacci sequence to $\sqrt{2}+2$. The arc chord length of Fibonacci spiral is obtained using Equation 13. Interestingly, the $C_{l\text{-}quad}$ obtained from Equation 13, forms the Pythagoras spiral. **Theorem 3.2.** The consecutive line segments of Pythagoras spiral (P_l) as manifested in Figure 9 can be also numerated using Equation 14 based on $Dl_{p\text{-}sq}$. Where, $C_{l-quad} = \left(\sqrt{2}+2\right) \times Dl_{p-sq} = P_l$. Table 2 reports the line segments of Pythagoras spiral using the proposed conjecture.

$$C_{l-qua} = \frac{r}{\left(\sqrt{2}+2\right)} \times \left(\left(\sqrt{2}+1\right) \times 2\right) \quad (13)$$

$$C_{l-qua} = \frac{1}{\left(\sqrt{2}+2\right)} \times \left(\left(\sqrt{2}+1\right) \times 2\right) = 1.41421$$

$$C_{l-qua} \equiv P_l = \left(\sqrt{2}+2\right) \times Dl_{P-sq} \quad (14)$$

$$C_{l-qua} \equiv P_l = \left(\sqrt{2}+2\right) \times 0.414 = 1.414$$

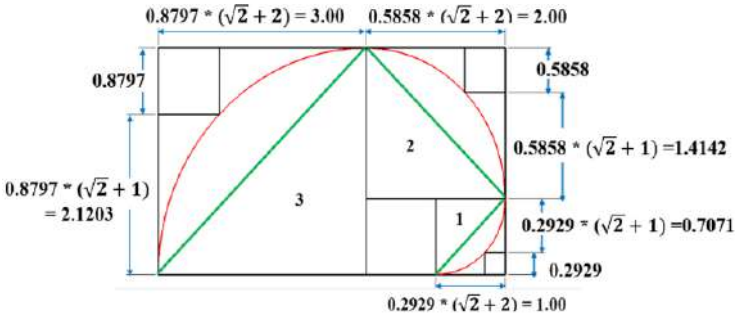

Fig 9: The properties of $\sqrt{2}$ conjecture in Fibonacci spiral.

Table 2. Pythagoras spiral based on proposed conjecture.

Term	Primary square	Pythagoras spiral length
1	0.2929 * $\sqrt{2}$ = 0.4142	0.4142 * $\sqrt{2}$ + 2 = 1.4142
2	0.5858 * $\sqrt{2}$ = 0.8284	0.8284 * $\sqrt{2}$ + 2 = 2.8284
3	0.8797 * $\sqrt{2}$ = 1.244	1.2440 * $\sqrt{2}$ + 2 = 4.2475
5	1.4655* $\sqrt{2}$ = 2.0725	2.0725 * $\sqrt{2}$ + 2 = 7.0759

Proof. A primary square with edge length of 15 is utilized to construct Fibonacci spiral configuration as shown in Figure 10. The dimension of the secondary overlapping square is determined using Equation 15-16. The following primary square on the adjacent side is determined by using Equation 17. Table 3 reports the convergence of the sequence to golden ratio. Factoring of any number as constant to Fibonacci sequence produces spiral configuration and ratios converging to golden ratio. However, the properties of the primary square can only be obtained by $\sqrt{2}$ conjecture.

$$X_n = (X_{n+1} + X_{n-2}) * \left(\sqrt{2}+2\right) \quad (15)$$

$$Secondary\ overlapping\ square\ edge\ length = \left(\sqrt{2}+2\right) * 15 = 51.2132 \quad (16)$$

$$Adjacent\ square\ edge\ length = (15+15)*\left(\sqrt{2}+2\right) = 102.426 \quad (17)$$

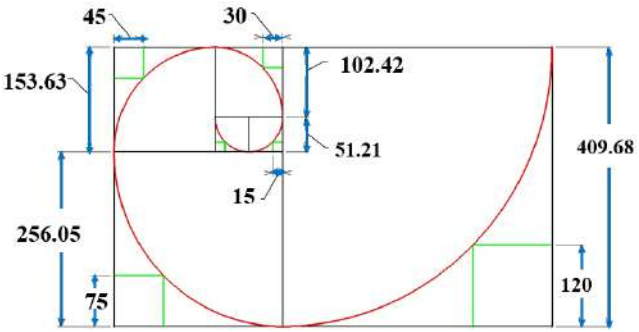

Fig 10: Constructed Fibonacci spiral based on $\sqrt{2}$ conjecture.

Table 3. Spiral configuration relative to Fibonacci sequence and $\sqrt{2}$ conjecture.

(n_{th})	Sequence $\sqrt{2}+2$	Ratio
1	15.0 * √2 + 2 = 51.21	51.21/51.21 = 1.00000
2	(15+15) * √2 + 2 = 102.42	102.42/51.21 = 2.00000
3	(30+15) * √2 + 2 = 153.63	153.63/102.42 = 1.50000
4	(45+30) * √2 + 2 = 256.05	256.05/153.63 = 1.66667
5	(75+45) * √2 + 2 = 409.68	409.68/256.05 = 1.60000
6	(120+75) * √2 + 2 = 665.73	665.73/409.68 = 1.62500
7	(195+120) * √2 + 2 = 1075.41	1075.41/665.73 = 1.615385
8	(315+195) * √2 + 2 = 1741.14	1741.14/1075.41 = 1.61905
9	(510+315) * √2 + 2 = 2816.55	2816.55/1741.14 = 1.61764
10	(825+510) * √2 + 2 = 4557.69	4557.69/2816.55 = 1.61818
11	(1335+825) * √2 + 2 = 7374.24	7374.24/4557.69 = 1.61797

3.3 Blade construction

Figure 11 illustrates the constructed blade morphology based on the proposed mathematical conjecture. Previous study shows that reduction in blade height improves the performance of the turbine. The proposed mathematical conjecture is utilized to construct Savonius wind turbine blade. As shown in Figure 11, the rotor diameter is set as the domain for the construction of the blades. Figure 12 shows the blade construction methodology at different curvature configuration. The first arc of the proposed blade is constructed based on the value obtained from ($\sqrt{2}$ + 2) by rotor diameter. Meanwhile the secondary curvature of the blade is formed based on the straight-line connection from point *A* to *B*. The line segment $\overline{AB}$ acts as the centreline for the construction of an arc, which acts as the control point for the formation of the blade curvatures. Line $\overline{DB}$ is taken as the maximum height reference for the blade curvature. Line $\overline{CO}$ is perpendicular to line $\overline{AB}$. Hence segment *AEB* is formed as shown in Figure 12. Arc *EB* is divided into 6 equidistant segments which act as the tangential line for the formation of the arcs. The segmentation process of the composite *ACB*, is methodologically reduced by ratio from $\sqrt{2}$ to approximately 1, meaning that the ratio of the line segment $\overline{AC}$ to the line $\overline{AB}$ is $\sqrt{2}$ and evenly reduced by ratio until approximately 1. Hence with this procedure, multiple secondary blade curvature can be obtained. For simplicity, randomly selected arc curvature which is highlighted in red is chosen for CFD analysis.

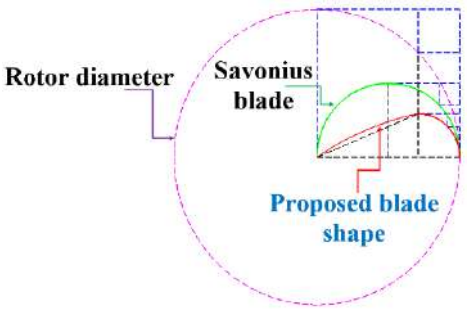

Fig 11: Comparison on proposed blade shape and standard Savonius turbine blade.

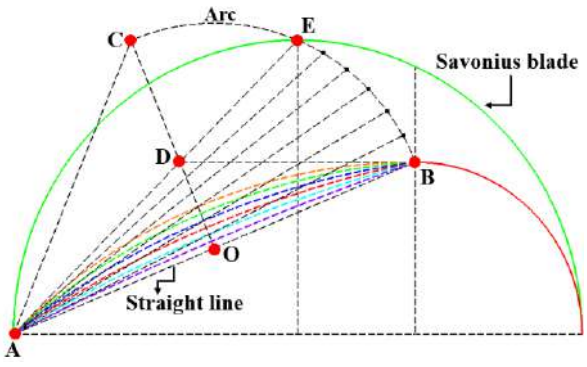

Fig 12: Proposed blade construction.

3.4 CFD configuration

CFD analysis is carried out in 2D configuration based on finite volume method (FVM) [46]. The aim of the computational methodology is to investigate the

aerodynamic properties of the proposed morphology in comparison to conventional SWT blade shape via Ansys Fluent 16.0. CFD technique computes Navier-Stokes equation to obtain flow field properties namely continuity equation as shows in Equation 19. In order to be cost effective in terms of computational power, widely utilized numerical strategy is adapted namely Reynolds-Averaged Navier Stokes Equation (RANS). Equation 18 shows Reynolds decomposition numerical model. The simulation is conducted using pressure-based solver assuming the flow is incompressible. Meanwhile, for turbulent transport model sensitivity, the turbine model is simulated using renormalized group (RNG), shear stress transport (SST) and standard k-ω. Ashwindran et al., (2020) reported that (SST) and standard k-ω exhibited trivial dissimilarities and stable numerical oscillation [21]. However, RNG did not agree well with other two models. Hence, SST *k-ω* is chosen for the rest of the simulation due to its robust feature. Moreover, pertaining to WT simulation SST *k-ω* is widely preferred by researcher, due to its blending feature as shown in Equation 20-21. Neumann boundary condition type is applied under the influence of constant U_∞ = 8 m/s. The bounding domain wall is set to symmetry and outlet pressure to 0-pascal gauge pressure. Operating pressure is set to 101.325 kPa [47]. Table 4 shows the boundary condition utilized for the CFD investigation. Figure 13 (a) and (b) shows the 2D CFD rotating domain configuration of Savonius WT and proposed morphology respectively.

Reynolds decomposition

$$u(x,y,t) = \overline{u}(x,y) + u'(x,y,t) \tag{18}$$

Conversation of mass or continuity equation,

$$\frac{\partial}{\partial x_i}\left(\overline{u_i} + u_i'\right) = 0 \tag{19}$$

Turbulent kinetic energy, *k*-equation

$$\frac{\partial k}{\partial t} + U_j \frac{\partial k}{\partial x_j} = P_k - \beta^* k\omega + \frac{\partial}{\partial x_j}\left[(\upsilon + \sigma_k \nu_T)\frac{\partial k}{\partial x_j}\right]$$

(20)

Specific rate of dissipation of kinetic energy, *ω*-equation

$$\frac{\partial \omega}{\partial t} + U_j \frac{\partial \omega}{\partial x_j} = aS^2 - \beta\omega^2 + \frac{\partial}{\partial x_j}\left[(\nu + \sigma_\omega \nu_T)\frac{\partial \omega}{\partial x_j}\right] + 2(1 - F_1)\sigma_{\omega^2}\frac{1}{\omega}\frac{\partial k}{\partial x_i}\frac{\partial \omega}{\partial x_i}$$

(21)

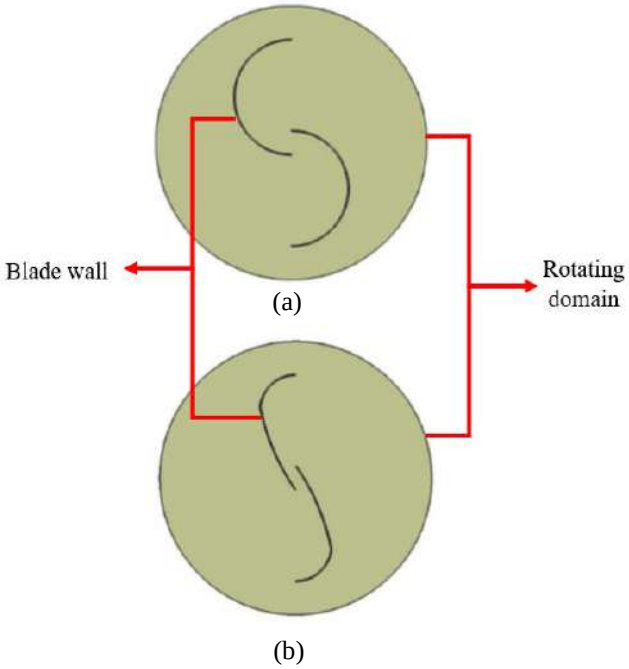

Fig 13: (a) Savonius WT, (b) Proposed morphology.

In terms of grid sensitivity, the discretized mesh topology is investigated under fine and medium densities. Results presented by Ashwindran et al., (2020) [21] shows that fine and medium mesh densities indicated trivial dissimilarities in terms of moment coefficient (C_m) at λ = 0.59. Therefore, medium mesh configuration is chosen for the rest of the simulation. In this study the grid topology of both turbines is discretized into static and dynamic domains using non-conformal mesh technique. Hence, sliding mesh method (SMM) is adapted in order to initiated rotation of the dynamic domain subjected to the defined rpm values. The WTs is subject to constant wind speed, U_∞ = 8 m/s at 100 and 160 rpm. The numerated tip speed ratio using Equation 22 is λ = 0.59 and λ = 0.94 at respective rpm. The preliminary aim of the research is to evaluate the moment coefficient properties of the turbines subjected to defined parameters. Therefore, moment coefficient of the computational WTs is numerated based on Equation 23.

Tip speed ratio

$$\omega = 2\pi f = 2\pi\left(rpm/60\right)$$

$$\lambda = \frac{\omega \times \left(\frac{D_r}{2}\right)}{U_\infty} \tag{22}$$

Moment coefficient

$$C_m = \frac{M}{\frac{1}{4}\rho S_A U_\infty^2 D_b} \tag{23}$$

Table 4. Boundary condition on 2D CFD analysis of proposed and SWT turbine.

Boundary condition	Parameter	Value
Boundary condition type	Neumann condition	-
Zone condition	Air @ 23 ° C	ρ = 1.2041 kg / m^3
Inlet	Constant velocity, U_∞	8 m/s
Surrounding wall type	Symmetry	-
Outlet	Pressure outlet	0-pascal gauge pressure
Turbulent viscosity, T_v	Typical medium turbulent condition	10 %
Turbulent intensity, I	Typical medium turbulent condition	5 %

Since information on I and turbulent viscosity (T_v) is unavailable the values are maintained at default value indicating medium turbulence scenario. It is recommended to utilize the default values for I and T_v as it represents a typical medium turbulent case [48]. The computed parameter is C_m with reference area of 0.9 m^2. Table 5 represents the parameters on solver configuration. Couple scheme is utilized for pressure-velocity coupling process. The residual imbalance criteria for governing equations are set to 10^{-5}. In terms of spatial discretization, k_t is set to second order upwind. Moreover, in order to make it less computationally expensive, the courant number (CFL) is set to 10 and time-step to 0.01 for 4 complete revolutions. Similar simulation configuration can be found in research conducted by Takeyeldein et al., (2020)[49] pertaining to WT CFD analysis.

Table 5. Solver configuration.

Solver configuration	Parameter	Value
State	Fixed time-step transient state	-
Continuity, Momentum and energy Solver	Pressure based solver	Incompressible flow
Turbulent transport model	SST k-ω	-
Velocity formulation	Absolute	-
Pressure-velocity coupling	Couple scheme	Second order upwind for k_t.
Residual imbalance criteria	Convergence criteria	10^{-5}
Number of revolutions	-	4
Time-step	Fixed time step	0.01

4. Result and discussion

Results shows that the proposed morphology has improved the performance in moment coefficient (C_m) by 7.2 % at λ = 0.59 and 4 % at λ = 0.94 in comparison to conventional SWT as shown in Table 6. Meanwhile, the pressure distribution of the proposed design and SWT along the blade region at different angular position namely 0º, 45º and 90º. At 0º, the pressure distribution on the concave side of SWT is higher than the proposed shape. However, at 0º, the suction pressure region behind the blade of the proposed shape is higher and denser than SWT. Suction pressure is negative pressure between two points of a region which cause the fluid to drawn from high to low pressure. As the angular position shifts to 45º the pressure distribution along the proposed advancing blade increases with less denser suction pressure region behind the blade in comparison SWT. This is due to the morphology of the blade as the fluid distributes along the blade region. It is observed that at 45º, proposed shape started to exhibit higher C_m than SWT. This is due to the concentred pressure distribution on tip side and lower blade height of the proposed blade in comparison to SWT. This consequently produces higher moment as tip of the blade is further from axis of the rotation, unlike semi-circle SWT the tip is at center of the shape and the blade height is greater than the proposed shape. Meanwhile at 90º angular position, both blades indicated similar flow properties which is high pressure region at convex side of returning blade and low-pressure region at blade tips. However, the proposed shape indicated higher pressure than SWT due to its sharp edge at the blade curvature. Self-staring issue can be obverse in the presented contours, as the advancing blade of each design requires high pressure or drag force to initiate the rotation. Comprehensive information on simulation configuration and flow results can be found in the article previously published by Ashwindran et al., (2020) [21].

Table 6. Average moment coefficient at λ = 0.59 and λ = 0.94.

Turbines	Average C_m at λ =0.59	Average C_m at λ=0.94
Savonius	0.375023	0.199312
Proposed	0.401881	0.207343

Conclusion

In this paper, the governing numerical factor for the construction of circles and Fibonacci spiral is investigated. The extracted numerical conjecture is adapted for the construction of DIWT relative to Savonius design configuration. It is found that the proposed conjecture $(\sqrt{2}+2)$ provides an alternative approach in parametrically constructing DIWT blade morphology. The effectiveness of the proposed blade is analyzed via CFD in terms of C_m. Previously conducted CFD result shows

that the constructed blade morphology based on the conjecture has improved C_m by 7.2 % at λ = 0.59 and 4 % at λ = 0.94 in contrast to conventional SWT. It appears that irrational number $\sqrt{2}$ is fundamental in the creation of circle and spiral. In addition, multiple combination of blade curvatures is also possible to be constructed with the newly found conjecture.

Acknowledgements

This research work was conducted under Fundamental Research Grant Scheme FRGS/1/2019/TK10/UMP/02/4 (RDU1901131). We would like to thank Ministry of Higher Education, Malaysia for making this research possible.

Nomenclature

c_m	Moment coefficient
U_∞	Free stream velocity (m/s)
I	Turbulent intensity
T_v	Turbulent viscosity (kg/m-s)
k_t	Turbulent kinetic energy (J/kg)
SST	Sheer stress transport
$L_{pr\text{-}sq}$	Length of primary square (m)
$C_{l\text{-}quad}$	Chord length quadrant (m)
$Dl_{p\text{-}sq}$	Diagonal length of the primary square (m)
P_l	Consecutive line segments of Pythagoras spiral (m)
D_r	Rotor diameter (m)
f	Frequency (Hz)
rpm	Revolution per minute
Fn	Fibonacci sequence
CFD	Computational fluid dynamics
RANS	Reynolds Averaged Navier Stokes
SMM	Sliding mesh method
FVM	Finite volume method
SWT	Savonius wind turbine
CFL	Courant number

Greek symbols

ρ	Density (kg/m^3)
ϕ	Golden ratio
π	22/7
ω	Specific turbulent dissipation rate (1/s)
λ	Tip speed ratio

References

1) R. Menzel, “Memory in the Bee,” in: J.D. Wright (Ed.), Int. Encycl. Soc. Behav. Sci., Second Edi, Elsevier, Oxford, 2015: pp. 155–159. doi:10.1016/B978-0-08-097086-8.51012-5.
2) J.H. Conway, H. Burgiel, and C. Goodman-Strauss, “The Symmetries of Things,” CRC Press, 2016. https://books.google.com.my/books?id=Drj1CwAAQBAJ.
3) S.-K. Lin, “Correlation of entropy with similarity and symmetry,” *J. Chem. Inf. Comput. Sci.*, **36** (*3*) 367–376 (1996). doi:10.1021/ci950077k.
4) A. Negi, A. Garg, and A. Agrawal, “Construction of 3d mandelbrot set and julia set,” *Int. J. Comput. Appl.*, **85** (*15*) 32–36 (2014). doi:10.5120/14920-3514.
5) H. Werner, “Symmetry As A Developmental Principle In Nature And Art,” World Scientific Publishing Company, 1998. https://books.google.com.my/books?id=_OnsCgAAQBAJ.
6) V. Nikolić, L. Radović, and B. Marković, “Symmetry of ‘twins,’” *Symmetry (Basel).*, **7** (*1*) 164–181 (2015). doi:10.3390/sym7010164.
7) M. Gaitán, C. Portalés, J. Sevilla, and E. Alba, “Applying axial symmetries to historical silk fabrics: silknow’s virtual loom,” *Symmetry (Basel).*, **12** (*5*) 742 (2020). doi:10.3390/sym12050742.
8) E.H. Cohen, and Q. Zaidi, “Symmetry in context: salience of mirror symmetry in natural patterns,” *J. Vis.*, **13** (*6*) 22–22 (2013). doi:10.1167/13.6.22.
9) H. Weichselbaum, H. Leder, and U. Ansorge, “Implicit and explicit evaluation of visual symmetry as a function of art expertise,” *Iperception.*, **9** (*2*) 204166951876146 (2018). doi:10.1177/2041669518761464.
10) Z. Xie, “The golden ratio and super central configurations of the n-body problem,” *J. Differ. Equ.*, **251** (*1*) 58–72 (2011). doi:10.1016/j.jde.2011.03.002.
11) S.K. Sen, and R.P. Agarwal, “Conclusions,” in: S.K. Sen, R.P. Agarwal (Eds.), Zero, Elsevier, 2016: pp. 93–142. doi:10.1016/B978-0-08-100774-7.00005-3.
12) I. Crăciun, D. Inoan, D. Popa, and L. Tudose, “Generalized golden ratios defined by means,” *Appl. Math. Comput.*, **250** 221–227 (2015). doi:https://doi.org/10.1016/j.amc.2014.10.095.
13) S.K. Sen, and R.P. Agarwal, “Golden ratio in science, as random sequence source, its computation and beyond,” *Comput. Math. with Appl.*, **56** (*2*) 469–498 (2008). doi:10.1016/j.camwa.2007.06.030.
14) X. Pan, “Platinum ratio search versus golden ratio search,” *Omega*, **36** (*6*) 1053–1056 (2008). doi:10.1016/j.omega.2006.05.004.
15) I. Jaraiedi, and Z. Zhuang, “Determination of optimal design parameters of $\bar{x}$ charts when there is a multiplicity of assignable causes,” *J. Qual. Technol.*, **23** (*3*) 253–258 (1991). doi:10.1080/00224065.1991.11979331.
16) S.M. Disney, D.R. Towill, and W. van de Velde, “Variance amplification and the golden ratio in production and inventory control,” *Int. J. Prod. Econ.*, **90** (*3*) 295–309 (2004).

doi:10.1016/j.ijpe.2003.10.009.
17) Harinaldi, Muhammad Denni Kesuma, R. Irwansyah, J. Julian, and A. Satyadharma, "Flow control with multi-dbd plasma actuator on a delta wing," *Evergreen*, **7** (*4*) 602–608 (2020). doi:10.5109/4150513.
18) Yanuar, Ibadurrahman, A. S. Pamitran, Gunawan, and S. Mau, "Experimental investigation on the spiral pipe performance for particle-laden liquids," *Evergreen*, **7** (*4*) 580–586 (2020). doi:10.5109/4150509.
19) M. Papaelias, and F.P.G. Márquez, "Wind turbine inspection and condition monitoring," in: M. Papaelias, F.P.G. Márquez, A.B.T.-N.-D.T. and C.M.T. for R.E.I.A. Karyotakis (Eds.), Non-Destructive Test. Cond. Monit. Tech. Renew. Energy Ind. Assets, Elsevier, Boston, 2020: pp. 19–29. doi:10.1016/B978-0-08-101094-5.00002-2.
20) N. Mohd, M.M. Kamra, M. Sueyoshi, and C. Hu, "Lattice boltzmann method for free surface impacting on vertical cylinder : a comparison with experimental data," *Evergreen*, **4** (*2/3*) 28–37 (2017). doi:10.5109/1929662.
21) S.N. Ashwindran, A.A. Azizuddin, and A.N. Oumer, "A moment coefficient computational study of parametric drag-driven wind turbine at moderate tip speed ratios," *Aust. J. Mech. Eng.*, 1–15 (2020). doi:10.1080/14484846.2020.1714364.
22) S. Saraf, and P. Saraf, "The golden proportion: key to the secret of beauty," *Internet J. Plast. Surg.*, **9** (*1*) (2013). doi:10.5580/2ce6.
23) A. Wares, "The golden ratio and regular hexagons," *Int. J. Math. Educ. Sci. Technol.*, **51** (*1*) 157–160 (2020). doi:10.1080/0020739X.2019.1587531.
24) K. Shekhawat, "Why golden rectangle is used so often by architects: a mathematical approach," *Alexandria Eng. J.*, **54** (*2*) 213–222 (2015). doi:10.1016/j.aej.2015.03.012.
25) C. Falbo, "The golden ratio: a contrary viewpoint," *Coll. Math. J.*, **36** (*2*) 123 (2005). doi:10.2307/30044835.
26) G. Vincenzi, and S. Siani, "Fibonacci-like sequences and generalized pascal's triangles," *Int. J. Math. Educ. Sci. Technol.*, **45** (*4*) 609–614 (2014). doi:10.1080/0020739X.2013.851806.
27) T.O. Omotehinwa, "Fibonacci numbers and golden ratio in mathematics and science," *Int. J. Comput. Inf. Technol.*, (*July 2013*) 631–638 (2013). https://www.researchgate.net/publication/334015286_Fibonacci_Numbers_and_Golden_Ratio_in_Mathematics_and_Science.
28) D. Andrica, V. Crişan, and F. Al-Thukair, "On fibonacci and lucas sequences modulo a prime and primality testing," *Arab J. Math. Sci.*, **24** (*1*) 9–15 (2018). doi:10.1016/j.ajmsc.2017.06.002.
29) Z.-W. Sun, "Fibonacci numbers and fermat's last theorem," *Acta Arith.*, **60** (*4*) 371–388 (1992). doi:10.4064/aa-60-4-371-388.
30) K. Kuhapatanakul, "The fibonacci p-numbers and pascal's triangle," *Cogent Math.*, **3** (*1*) 1264176 (2016). doi:10.1080/23311835.2016.1264176.
31) F. Fang, R. Aschheim, and K. Irwin, "The unexpected fractal signatures in fibonacci chains," *Fractal Fract.*, **3** (*4*) 49 (2019). doi:10.3390/fractalfract3040049.
32) J.B. Gil, and A. Worley, "Generalized metallic means," *Fibonacci Q.*, **57** (*1*) 45–50 (2019). http://arxiv.org/abs/1901.02619.
33) Z. Li, W. Zhang, H. Dong, and Y. Tian, "Performance analysis and structure optimization of a nautilus isometric spiral wind turbine," *Energies*, **13** (*1*) 120 (2019). doi:10.3390/en13010120.
34) Y. Patil, "Design, fabrication and analysis of fibonacci spiral horizontal axis wind turbine," *Int. J. Aerosp. Mech. Eng.*, **5** (*2*) 19–22 (2018).
35) Q. Lu, Q. Li, Y.-K. Kim, and K.-C. Kim, "A study on design and aerodynamic characteristics of a spiral-type wind turbine blade," *J. Korean Soc. Vis.*, **10** (*1*) 27–33 (2012). doi:10.5407/JKSV.2011.10.1.027.
36) W. Monatrakul, and R. Suntivarakorn, "Effect of blade angle on turbine efficiency of a spiral horizontal axis hydro turbine," *Energy Procedia*, **138** 811–816 (2017). doi:10.1016/j.egypro.2017.10.075.
37) J. Aubin, I. Naude, J. Bertrand, and C. Xuereb, "Blending of newtonian and shear-thinning fluids in a tank stirred with a helical screw agitator," *Chem. Eng. Res. Des.*, **78** (*8*) 1105–1114 (2000). doi:10.1205/026387600528382.
38) R. Suntivarakorn, S. Wanchat, and W. Monatrakul, "An experimental study of electricity generation using a horizontal spiral turbine," *Energy Procedia*, **100** (*September*) 532–536 (2016). doi:10.1016/j.egypro.2016.10.215.
39) E. Antar, and M. Elkhoury, "Parametric sizing optimization process of a casing for a savonius vertical axis wind turbine," *Renew. Energy*, **136** 127–138 (2019). doi:10.1016/j.renene.2018.12.092.
40) J. He, X. Jin, S. Xie, L. Cao, Y. Wang, Y. Lin, and N. Wang, "CFD modeling of varying complexity for aerodynamic analysis of h-vertical axis wind turbines," *Renew. Energy*, **145** 2658–2670 (2020). doi:10.1016/j.renene.2019.07.132.
41) Y. Celik, L. Ma, D. Ingham, and M. Pourkashanian, "Aerodynamic investigation of the start-up process of h-type vertical axis wind turbines using cfd," *J. Wind Eng. Ind. Aerodyn.*, **204** (*May*) 104252 (2020). doi:10.1016/j.jweia.2020.104252.
42) S. Mauro, S. Brusca, R. Lanzafame, and M. Messina, "CFD modeling of a ducted savonius wind turbine for the evaluation of the blockage effects on rotor performance," *Renew. Energy*, **141** 28–39 (2019). doi:10.1016/j.renene.2019.03.125.
43) S.J. Deshmukh, "Design and development of vertical axis wind turbine," (*July 2017*) (2018). doi:10.21013/jte.ICSESD201728.
44) K. Rogowski, and R. Maroński, "CFD computation of the savonius rotor," *J. Theor. Appl. Mech.*, **53** (*1*)

37–45 (2015). doi:10.15632/jtam-pl.53.1.37.
45) A. Fiorenza, and G. Vincenzi, “From fibonacci sequence to the golden ratio,” *J. Math.*, **2013** 1–3 (2013). doi:10.1155/2013/204674.
46) N. Mohd, M.M. Kamra, M. Sueyoshi, and C. Hu, “Three-dimensional free surface flows modeled by lattice boltzmann method : a comparison with experimental data,” *Evergreen*, **4** (*1*) 29–35 (2017). doi:10.5109/1808450.
47) O.M.A.M. Ibrahim, and S. Yoshida, “Experimental and numerical studies of a horizontal axis wind turbine performance over a steep 2d hill,” *Evergreen*, **5** (*3*) 12–21 (2018). doi:10.5109/1957496.
48) A.M.M. Ismaiel, and S. Yosida, “Study of turbulence intensity effect on the fatigue lifetime of wind turbines,” *Evergreen*, **5** (*1*) 25–32 (2018). doi:10.5109/1929727.
49) M.M. Takeyeldein, T.M. Lazim, I.S. Ishak, N.A.R. Nik Mohd, and E.A. Ali, “Wind lens performance investigation at low wind speed,” *Evergreen*, **7** (*4*) 481–488 (2020). doi:10.5109/4150467.